Key Points:

- Field line resonances (FLRs) with polarization between poloidal/toroidal (3-D) form at azimuthal gradients in the Alfvén speed
- Simulations show these will occur prominently at the boundaries of the dusk-side plasmaspheric drainage plume
- We present observable phase, amplitude, and polarization characteristics for use in the identification of 3-D FLRs in data

Correspondence to:
T. Elsden,
thomas.elsden@glasgow.ac.uk

Polarization Properties of 3-D Field Line Resonances

T. Elsden[1,2] and A. N. Wright[3]

[1]School of Mathematics and Statistics, University of Glasgow, Glasgow, UK, [2]School of Physics and Astronomy, University of Leicester, Leicester, UK, [3]School of Mathematics and Statistics, University of St Andrews, St Andrews, UK

Abstract Recent work has shown that field line resonances (FLRs) can form with intermediate magnetic field polarizations, that is, between toroidal (azimuthal) and poloidal (radial). In this case, they are referred to as "3-D", given that the equilibrium and therefore associated wave solutions vary in all three dimensions. Such 3-D variations in the medium can be expected in the magnetosphere in particular during the presence of a plasmaspheric drainage plume in the dusk flank. In this case, strong field-aligned currents driven by FLRs can form along contours of Alfvén frequency which are very asymmetric azimuthally. In this study, we use magnetohydrodynamic (MHD) simulations performed in a background dipole magnetic field, to consider what the satellite signatures would be for a spacecraft observing such non-toroidal FLRs under different magnetopause driving conditions. We consider how the 3-D nature impacts the amplitude and phase relations traditionally expected for FLRs. We find that in the 3-D FLR regions of intermediate polarization, the FLR has strong contributions from both the radial and azimuthal field components (velocity, magnetic or electric) and these are in or out of phase. We show how hodograms can be used to infer the FLR polarization in these cases as well as provide predictions for the variation of the FLR polarization with MLT across a plasmaspheric plume. We further show how the presence of a significant global fast mode can skew the resulting polarization estimates.

Plain Language Summary The Earth sits in the constantly streaming outflow from the Sun known as the solar wind, and is protected from the bombardment of charged particles by its magnetic field. This forms a cavity within the solar wind, known as the magnetosphere, similar to the way in which the flow of a river deviates around a large rock. This cavity supports natural modes of oscillation, very much like the harmonics of sound waves in a musical instrument. Therefore when the magnetosphere is impacted by the dynamic solar wind, the magnetosphere vibrates. The resulting oscillations (known as ultralow frequency [ULF] waves), transfer energy throughout the system and can reveal key information about the magnetospheric environment. In this work, we use a computer simulation to study a particular ULF wave process, known as field line resonance (FLR). This process generates field-aligned currents, which impact the generation of the aurora. The novelty of this work is considering the process of FLR in a fully 3-D system. Using the simulation results, we predict the wave signatures which would be expected to be seen from this process in satellite and ground-based instrumentation.

1. Introduction

Ultra-low frequency (ULF) waves (∼1 mHz–1 Hz; Jacobs et al., 1964) represent the lowest frequency oscillations of the magnetosphere, transferring energy and momentum throughout the system. On the lower end of this frequency spectrum, magnetohydrodynamic (MHD) fast and Alfvén waves are the dominant modes of oscillation of the cold magnetospheric plasma. Such modes have a rich history of study in Earth's magnetosphere, with Dungey (1954) first connecting the continuous near-sinusoidal pulsations (Pc waves) observed on the ground with Alfvén waves standing along geomagnetic field lines. The latitudinal and amplitude variation of these waves observed by Samson et al. (1971) was explained by the process of field line resonance (FLR; Chen & Hasegawa, 1974; Southwood, 1974). This describes the coupling of fast and Alfvén waves in the inhomogeneous magnetosphere, occurring at the local field line whose Alfvén eigenfrequency matches that of the global fast wave. At this field line there is a resonance between the two modes, with energy being transferred from the fast to the Alfvén wave, the amplitude of which grows in time. When there is no azimuthal variation in the medium, the resulting Alfvén wave has a dominantly toroidal (azimuthal) polarization, with this nomenclature deriving from the magnetic not electric field polarization. This process has been extensively studied both analytically and numerically in Cartesian, cylindrical and dipolar coordinate systems (e.g., Allan et al., 1985, 1986; Kivelson &

Southwood, 1985, 1986; Lee & Lysak, 1989; Wright & Thompson, 1994). It has further been employed to explain a plethora of ULF wave observations (e.g., Hartinger et al., 2011; Mathie & Mann, 2000; Rae et al., 2005; Takahashi & McPherron, 1984; Walker et al., 1979).

The above studies created the classical picture of the FLR process, where the Alfvén frequency varies significantly in the radial direction through changes in the plasma mass density, magnetic field strength and the field line length. However, in the magnetosphere, there are also significant variations in the density with local time (to be elucidated below). This requires variation in an extra (third) spatial dimension to be considered than had been treated previously. Studies by Lee et al. (2000) and Russell and Wright (2010) investigated in a Cartesian box geometry the effect of an azimuthal density variation on the FLR process. They found that FLR still occurs efficiently, with the resonance forming tangential to contours of Alfvén frequency. Therefore, the Alfvén wave can have a mixed polarization, between toroidal and poloidal. However, the Cartesian, straight magnetic field regime fails to account for a key property of the true magnetospheric situation. Namely, the poloidal and toroidal Alfvén frequencies differ substantially (by ∼30% for the fundamental) in a dipole magnetic field (Cummings et al., 1969; Radoski, 1967).

The ramifications of this difference were explored by Elsden and Wright (2017) and Wright and Elsden (2016) in an effort to put the 3-D FLR process on a firm theoretical footing. To be clear, by "3-D FLR" as referred to in the title of this study, we refer to the inhomogeneity of the plasma conditions (e.g., mass density or magnetic field variation) in three dimensions. These studies showed that, as a significant difference to the box model case, there is no longer a unique location where the resonant coupling occurs. In fact, in a fully 3-D medium there are infinite families of possible solutions to the resonance condition. These solutions can be mapped out as contours in the equatorial plane along which the resonance condition (Alfvén frequency equal to driving frequency) is satisfied. This can be envisaged by realizing that Alfvén waves at different radial locations can have the same Alfvén frequency by adopting a different polarization. This leads to the question of where resonances will form in an inhomogeneous medium for a given fast driving frequency.

Other studies have touched on similar issues from slightly different standpoints. Degeling et al. (2010), Kabin, Rankin, Mann, Degeling, & Marchand (2007), and Kabin, Rankin, Waters, et al. (2007) explored the polarization properties of FLRs in a non-axisymmetric equilibrium using a compressed dipole background magnetic field. They identified different solution paths (for constant Alfvén frequency) along which the Alfvén wave polarization varies significantly with magnetic local time, in conceptual agreement with the results of Wright and Elsden (2016). Furthermore, Klimushkin et al. (1995) and Leonovich and Mazur (1993) considered standing Alfvén waves in 3-D non-uniform equilibria, showing that the polarization for a given frequency can be anywhere between poloidal and toroidal.

The 3-D nature of FLRs is expected to be most prominent, that is, with a substantial deviation from a toroidal polarization, during periods of significant azimuthal asymmetry within the magnetosphere. Such asymmetry arises starkly during the formation of a dusk-side extension of the plasmasphere, prevalent during geomagnetic storms, known as a plasmaspheric drainage plume (e.g., Goldstein et al., 2005; Moldwin et al., 2016; Sandel et al., 2003). During enhanced magnetospheric convection as typical of storm time conditions, the plasmasphere drains, with cold dense plasma flowing toward the dayside magnetopause forming the dusk-side plume structure. Such plumes can be long-lived, often lasting for four days or more (Borovsky & Denton, 2008), but sometimes lasting for weeks (Borovsky et al., 2014). Given that the dawn and dusk edges of the plume structure have sharp azimuthal density gradients, they are ideal candidates for the investigation of 3-D FLR structures. Indeed, the simulations of Degeling et al. (2018) and Wright and Elsden (2020) show clearly how 3-D FLRs can form at such density gradients.

The aim of this article is to investigate the properties of 3-D FLRs and to identify observable features to be looked for in ground and spacecraft data. The polarization analysis of THEMIS satellite observations of FLRs by (Sarris et al., 2009, 2010) demonstrates well how satellite data could be used to look for 3-D FLRs. The intermediate Alfvén wave polarizations expected at the steep azimuthal density gradients raise the question of the interpretation of ULF wave observations as either poloidal or toroidal modes, both of which are usually attributed to entirely different magnetospheric processes. For example, toroidal ULF waves are usually attributed to large azimuthal scale (so called "low-m", for azimuthal wavenumber m) processes for example, solar wind buffeting of the magnetopause and the Kelvin-Helmholtz unstable flank magnetopause. Poloidal or high-m ULF waves on the other
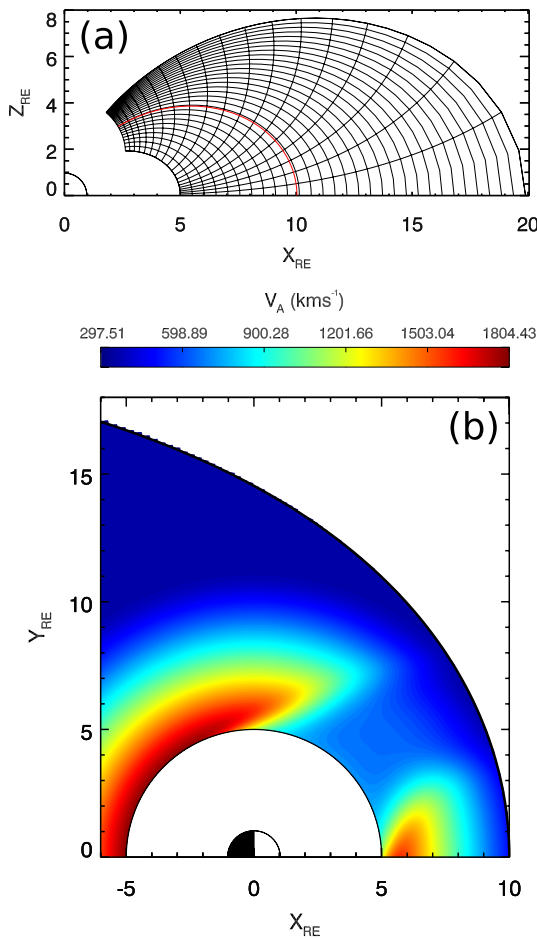
Figure 1. (a) Simulation grid in the noon meridional plane. Black lines are contours of the meridional and field-aligned coordinates. Note that not every contour is plotted. The red line indicates the magnetopause location for the noon meridian. (b) Alfvén speed in the equatorial plane.

hand are thought to be excited by resonance with energetic particles drifting around the Earth, through the drift or drift-bounce resonance mechanisms (Southwood et al., 1969). Understanding and predicting the expected polarization is further a critical quantity for the interaction with energetic radiation belt particles (Elkington et al., 2003; Kabin, Rankin, Mann, et al., 2007; Kabin, Rankin, Waters, et al., 2007). Furthermore, the resulting intermediate polarization, which will also be present in the field-aligned current (FAC) associated with the FLRs, will influence the spatial structure of any aurora generated by this mechanism (e.g., Milan et al., 2001; Rankin et al., 2005). Using numerical simulations of a plume equilibrium, we will test a variety of driving mechanisms (e.g., monochromatic, broadband, solar wind pressure pulse) and provide resulting virtual in-situ measurements of the wavefields. These will form predictions to be used for the future identification of 3-D FLRs in observations.

The article is structured in the following way: Section 2 summarizes the numerical model used for the simulations; Section 3 provides the results from each of the three types of magnetopause driving; Section 4 summarizes and concludes the study.

2. Numerical Model

We use the numerical model of Wright and Elsden (2020), which will be briefly summarized here. The model solves the linear MHD equations under the cold plasma approximation (zero β) in a background dipole magnetic field geometry. We use a second-order accurate (in time and space) Leapfrog-trapezoidal finite difference scheme for the solution (Zalesak, 1979). The simulation grid in the noon-meridional $X - Z$ plane is displayed in Figure 1a, showing contours of the meridional and field-aligned coordinates (not every contour is plotted). The outer magnetopause boundary is set by the empirical formula of Shue et al. (1997), with a subsolar standoff distance of 10_{RE}, which is indicated by the red line in Figure 1a. The grid plotted extends past this location to show how the resolution varies in the flank magnetosphere to larger radial distances. The solution domain only includes the northern hemisphere and dusk flank (i.e., a quarter of the overall magnetospheric volume) for numerical efficiency. Therefore symmetry conditions are used at the equator and the noon and midnight meridians.

Figure 1b displays the equilibrium Alfvén speed in the equatorial plane, which further provides a visual representation of the simulation domain. The Alfvén speed is chosen to have a significant depression on the dusk flank, as would be expected during the presence of a plasmaspheric drainage plume of enhanced density. The given form is chosen to provide the significant density gradients as expected for such plumes.

The inner boundary at $L = 5_{RE}$ is held perfectly reflecting, while on the outer magnetopause boundary the field-aligned magnetic field component $b_\parallel$ is perturbed to drive the system. This models driving the system with magnetic pressure, indicative of the response of the magnetosphere to driving by the solar wind dynamic pressure. The specific form of the driver in each simulation will be detailed in each of the upcoming results sections. The ionospheric boundary is also perfectly reflecting, modeling a perfectly conducting ionosphere. Evidently, this will neglect the effects of a changing ionospheric conductivity on the FLRs themselves (e.g., Lu et al., 2008), or the effect of including ionospheric structure such as the ionospheric Alfvén resonator (Streltsov & Huba, 2015).

Dissipation is included in the model in two ways. First, energy is lost to the tail through a dissipative buffer zone covering $-9_{RE} < X < -6_{RE}$, meaning that waves which reach this far boundary do not return to the solution domain of interest. This is enforced by adding a drag term, $-\nu\mathbf{u}$ for drag coefficient ν, to the equation of motion (please see Section 3.3 of Wright & Elsden, 2020 for further details). The spatial variation of ν is given by the expression:

$$\nu = \nu_0 \sin^2 \left(\frac{\pi}{2} \frac{X - X_1}{X_2 - X_1} \right) \qquad (1)$$

for $\nu_0 = 8.0$, $X_1 = -6_{RE}$ and $X_2 = -9_{RE}$, such that the drag increases smoothly toward the far simulation boundary. Second, resistivity is included to limit FLR widths such that they are always fully resolved. The resistivity is taken to be uniform over most of the domain, but is smoothly decreased to zero toward the ionospheric ends of the field lines, where the small grid spacing would lead to a small local diffusion timescale which would greatly increase simulation run times. The dimensionless value of the magnetic diffusivity in the uniform regions for most of the simulations performed is $\eta = 0.0001$, with one exception discussed around Figure 2d. With the following normalization: length $L_0 = 6.371$ km, time $T_0 = 6.371$ s, the dimensional magnetic diffusivity is $\eta = \tilde{\eta}\eta_0 = 637.1 \, \mathrm{km}^2\mathrm{s}^{-1}$. Full details of these settings are given in Section 3.4 of Wright and Elsden (2020).

Overall, this recently developed model is the perfect tool to assess the formation of 3-D FLRs at density gradients in the magnetosphere. Global magnetospheric MHD models (e.g., Claudepierre et al., 2016; Ellington et al., 2016) typically struggle to resolve the finer scales of the FLR process which form perpendicular to the field through Alfvén wave phase mixing. We utilize optimized dipole coordinates, which are derived to alleviate some of the grid spacing issues that come with standard dipole coordinates (Kageyama et al., 2006) and allow for unprecedented resolution. Please see Section 2 of Wright and Elsden (2020) for a full derivation of the orthogonal field-aligned coordinates, (α, β, γ), used in the model. Briefly, the γ coordinate is directed along the background field; β is the azimuthal coordinate, the same as the spherical coordinate ϕ; α is the meridional coordinate, normal to the magnetic field lines in a meridian and effectively labels L-shells. However, for most plots of measurements in the equatorial plane, we display the components in terms of the transverse spherical coordinates r and ϕ, as well as a component along the background field, referred to by the subscript $\parallel$, for a more intuitive understanding. In the simulations performed a grid consisting of $(\alpha_m = 300, \beta_m = 200, \gamma_m = 40)$ points was used, providing for example, a radial resolution of 0.05_{RE} in the equatorial plane. Energy conservation is checked in the code by calculating the total energy in the simulation domain at each timestep as well as the expected losses due to dissipation (through the buffer zone and resistivity). These are then added and the total found to be constant over the course of a simulation (once energy is no longer being inputted through the driver), to one part in 10^4 for a typical run.

3. Results

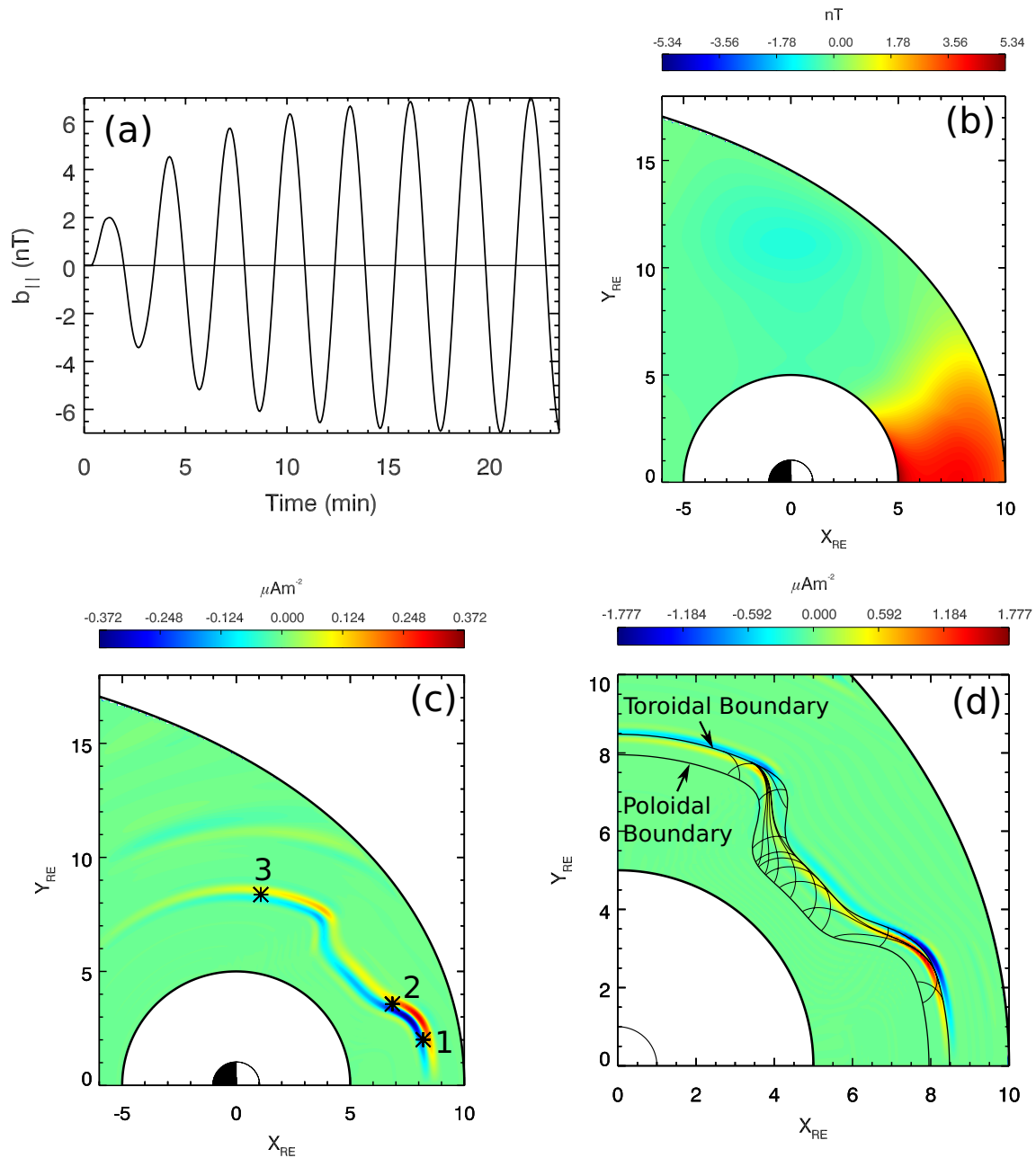### 3.1. Monochromatic Driver

We begin with the simplest driving mechanism such that the signals can be cleanly understood before looking at more realistic driving. The dominant linear component of the magnetic pressure ($b_\parallel$) is perturbed on the outer magnetopause boundary, monochromatically at 5.6 MHz. This is the fundamental waveguide frequency, found by initially driving the boundary with a broadband pulse, then taking the frequency spectrum of the resulting compressional signals within the waveguide. The full temporal and spatial dependence of the perturbation to $b_\parallel$ (b_γ in the simulation coordinates) on the magnetopause boundary can be expressed as:

$$b_\gamma(\beta, \gamma, t) = \cos^2(k_\beta \beta) \cos^2(k_\gamma \gamma) \sin(\omega_d t), \qquad (2)$$

for azimuthal coordinate β and field-aligned coordinate γ, where ω_d is the driving frequency. The azimuthal extent of the driving extends from noon to around 16MLT, where k_β is chosen to give a quarter azimuthal wavelength over this extent, after which the driver is turned off. The choice of the cosine dependence on azimuth provides an antinode at noon. In the field-aligned direction, it can be seen that the perturbation has a $\cos^2$ dependence. The chosen k_γ gives a full width at half maximum of 6_{RE} for the full field line length (3_{RE} for the half field line solved over). It should be noted that the azimuthal and field-aligned dependence of the driver is the same for all of the simulations in this study. From this point on in the manuscript, we will reference the field-aligned and azimuthal coordinates using $\parallel$ and ϕ subscripts respectively, for a more intuitive understanding.

Figure 2a displays the compressional magnetic field component within the waveguide at $(x, y, z) = (7.57, 0.0, 0.0)$ on the noon meridian, for driving at the natural fundamental waveguide frequency. The perturbation grows in time until saturated, when energy lost to the tail and to the FLR balances the input from the driven magnetopause. Isolating the waveguide frequency and driving with it monochromatically in this way ensures the cleanest possible signatures as there is only one frequency present. The spatial mode structure in the equatorial plane

Figure 2. Monochromatically driven simulation figures: (a) Waveguide response of $b_\parallel$ at $(x, y, z) = (7.57, 0.0, 0.0)$. (b) Contour plot of $b_\parallel$ in the equatorial plane at $t = 18.62$ min. (c) Field-aligned current $j_\parallel$ at the ionosphere, mapped to the equatorial plane at time $t = 22.83$ min. Asterisks at 1: $(x, y, z) = (8.20, 2.01, 0.0)$; 2: $(6.85, 3.57, 0.0)$; 3: $(1.08, 8.37, 0.0)$ give locations for further analysis. (d) Close-up of the region of strong $j_\parallel$ from (c), from a simulation with lower resistivity ($\eta = 2.5 \times 10^{-5}$) and therefore narrower FLR width and larger amplitude. Overlaid as the black lines is the Resonance Map, further described in main text.

for the compressional magnetic field at $t = 18.62$ min is given in Figure 2b. Given the symmetry of the driving condition about the Earth-Sun line, there is an antinode of $b_\parallel$ at noon. It can be seen that the nodal structure of the compressional magnetic field deforms to some degree around the plume. However, this study will not assess the details of the spatial compressional mode structure in the presence of a density plume, which will be the topic of future research.

In Figure 2c, the resulting FAC at the ionospheric ends of the field lines (indicative of the Alfvén wave response) is shown, mapped to the corresponding location in the equatorial plane, at $t = 22.83$ min. Numbered asterisks represent locations (listed in the figure caption) from where time series will be plotted in upcoming figures. A

clear resonant contour emerges, which turns sharply Earthward as the density gradient is crossed. On the dusk-ward edge of the plume, the resonant contour kinks radially outward to rejoin the same L-shell of field lines from which it started at noon. The excitation of a 3rd field-aligned harmonic can also be seen faintly on longer field lines at larger L. A similar FAC structure associated with a 3-D FLR in a density plume was shown in Figure 11 of Wright and Elsden (2020). Wright and Elsden (2016) showed that the plasma displacement will follow contours of Alfvén frequency, and therefore will have an intermediate polarization (between toroidal and poloidal) in the regions where the contours cross L-shells. In a dipole magnetic field, the toroidal and poloidal frequencies differ by approximately 30%. Therefore, the intermediate polarization adopted is such that the Alfvén wave at a given location and polarization matches the driving frequency.

A useful tool in understanding the shape of the enhanced current contours is the Resonance Map (Wright & Elsden, 2016), which represents solutions to the Alfvén wave equation for a given driving frequency that is, giving possible FLR locations. An extensive discussion on Resonance Maps and how to generate them is given in Sections 4.2 and 4.3 of Wright and Elsden (2016), but their significance will be briefly described here. The Resonance Map for the given equilibria and driving frequency is overlaid on top of a close-up of the FAC as Figure 2d. We performed a new simulation with a lower resistivity (reduced by a factor of four with dimensionless value of $\eta = 2.5 \times 10^{-5}$ compared to $\eta = 1 \times 10^{-4}$) to produce this plot, in order to narrow the resonance width and give a cleaner comparison to the Resonance Map contours. The outer and innermost black lines bound the Resonant Zone, which signifies the only region in which the Alfvén frequency can match the driving frequency (for the fundamental field-aligned mode). The outer thin black line is the toroidal boundary (labeled), meaning that along this line an Alfvén wave with a toroidal polarization will have a frequency matching the driving frequency. Similarly, the inner thin black line marks the poloidal boundary (labeled). The separation of these boundaries (i.e., size of the Resonant Zone) depends upon the difference in the poloidal and toroidal Alfvén frequencies and the Alfvén frequency gradient. It is clear that both boundaries deviate radially inwards upon crossing the plume boundaries: to match the driving frequency in the lower density region, the solution paths have to cross to shorter field lines at lower *L*.

The black lines between these boundaries represent permissible solutions (there are infinitely many) to the FLR condition, where the tangent to the curves at any given location gives the polarization required for the Alfvén frequency to match the driving frequency. These are traced by solving the Alfvén wave equation (Equation 9 from Singer et al., 1981) for intermediate polarizations at different locations (Equation 23 from Wright & Elsden, 2016). This is applicable for the background dipole magnetic field used here which can be described by an orthogonal coordinate system (Kabin, Rankin, Mann, et al., 2007; Kabin, Rankin, Waters, et al., 2007). The center of the current density enhancement (between blue and red peaks, though these peaks will cycle over the course of an Alfvén period) in the azimuthally invariant regions either side of the plume is well traced out by the toroidal boundary, as expected for a classical toroidally polarized FLR.

In the regions of steeper azimuthal Alfvén frequency gradient that is, around the plume boundaries, it is clear that several of the solutions converge to a particular solution path (e.g., at $(x, y) \sim (4, 7)$ and $(7.5, 3)_{RE}$). This solution matches well with the enhancement in the current density, but it is interesting to understand why this is the solution, when technically any one of the contours would be mathematically viable. Wright and Elsden (2016) showed that the boundary conditions and locally 2-D (azimuthally invariant) regions will "seed" the resulting solution path. As can be seen from Figure 2d, the dominant solution must be approximately toroidal in the middle of the plume, as well as on the noon and dusk sides of the plume, based on the negligible azimuthal variation of the medium in these regions. This forces the solution to be located at the toroidal boundary at these locations. This chooses the overall particular solution, which exits the toroidal boundary in the regions of sharp azimuthal variation and rejoins it once the medium returns to being azimuthally invariant (e.g., follow the contour leaving the toroidal boundary at $(x, y) \sim (5.75, 4)_{RE}$ and rejoining it at $(x, y) \sim (8, 2.75)_{RE}$). The fact that the FLR location from the 3-D simulation can be predicted from the Resonance Map, further highlights the utility of this theoretical tool, as well as providing invaluable insight as to why the FLR forms where it does.

Returning to the overall purpose of this work, the azimuthally non-uniform resonance structure shown in Figure 2c presents a new variability to ULF wave observations. The question that this study aims to answer is what would satellite signatures of such 3-D FLRs look like?
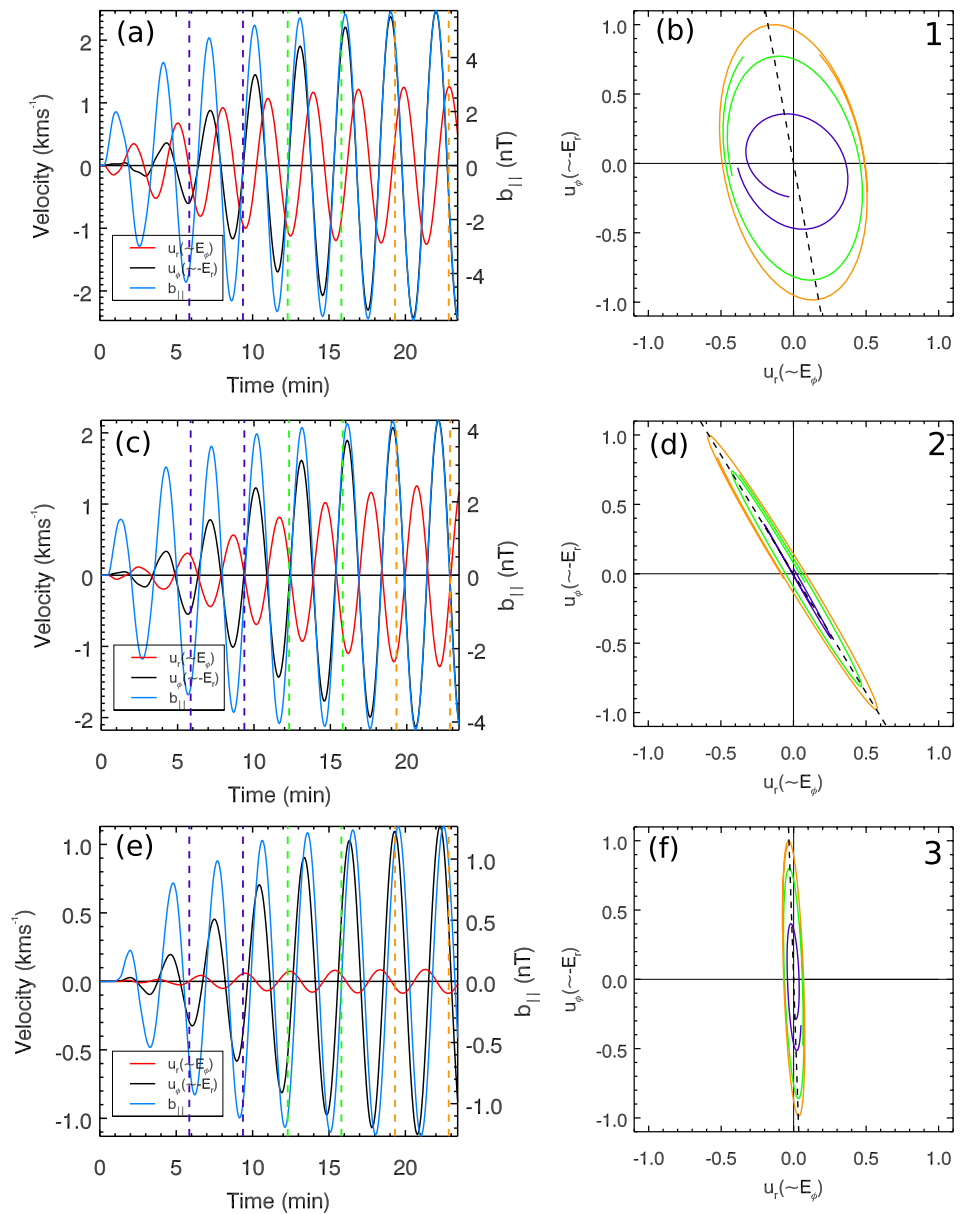
Figure 3. Time series and hodograms from the monochromatically driven simulation. (a) Time series for u_r (red), u_ϕ (black), $b_\parallel$ (blue) at $(x, y, z) = (8.20, 2.01, 0.0)$ (location labeled 1 in Figure 2c); (b) Hodograms for perpendicular velocity components u_r and u_ϕ, with colors corresponding to the time intervals given by the vertical dashed lines in (a). The dashed black line gives the major axis of the hodogram ellipse from the last time interval (orange). (c, d) Same as (a, b) for location 2 in Figure 2c, $(x, y, z) = (6.85, 3.57, 0.0)$ in the inclined FLR region. (e, f) Same as (a, b) for location 3 in Figure 2c), $(x, y, z) = (1.08, 8.37, 0.0)$ at the dusk side FLR.

Figure 3 displays time series (left) and hodograms (right) taken from the numbered asterisk locations shown in Figure 2c in the equatorial plane, with the corresponding number shown in the top right of the hodogram plots. In each of the left hand panels, the radial velocity (u_r-red), the azimuthal velocity (u_ϕ-black) and field-aligned magnetic field ($b_\parallel$-blue) perturbations are plotted, with the velocity axis on the left and the magnetic field axis on the right. The colored hodograms are taken from the corresponding time intervals between the vertical dashed colored lines in the time series figures. We have chosen to analyze the velocity in this study, as it gives a very intuitive understanding for 3-D FLRs, given that the velocity is polarized along the resonant contour. We realize however, that observers more often work with the electric or magnetic field components. The satellite locations

chosen are in the equatorial plane, where $b_\perp = 0$, so for comparison, we have highlighted the relationship between the velocity and electric field components on all relevant axis labels and legends.

The quantities in Figure 3a are plotted near noon, outside of the dense plume region where the FLR is approximately toroidally polarized (location 1, $(x, y, z) = (8.20, 2.01, 0.0)$). The azimuthal velocity (black) grows in time indicative of a driven FLR response. This growth is faster than, and saturates later than, that of the fast waveguide mode which can be seen in the radial velocity (red) and compressional magnetic field (blue) curves. The fast mode saturates due to loss to the tail and FLR, whereas the Alfvén response saturates due to the dissipation present through resistivity in the simulation. In this quasi-2-D (no azimuthal variation) FLR region, the contributions to the perpendicular velocity components of the fast and Alfvén waves can be easily separated, with the ordering from classical FLR theory (e.g., Southwood, 1974) holding such that the FLR fields satisfy $u_\phi \gg u_r$. However, the strong fast mode here (due to the waveguide being driven here at its natural frequency), adds significant amplitude to the radial velocity component. The velocity components are $\sim 90°$ out of phase, resulting in an elliptical hodogram in panel (b). The deviation of the major axis of the ellipse (dashed black line) from the toroidal direction is due to the presence of the fast mode having a significant radial velocity u_r.

Figure 3c shows the response at the intermediate FLR location (labeled 2 in Figure 2c at $(x, y, z) = (6.85, 3.57, 0.0)$). In this region, given that the plasma displacement aligns with the resonant contour, there is a substantial amount of the FLR response in u_r. This can be seen in the red curve in panel (c), which now continues to grow (similar to the black curve for u_ϕ) rather than saturating as in panel (a). The hodogram structure shown in panel (d) is also completely different due to the changed phase relation between u_r and u_ϕ (now in antiphase). Therefore the 2-D ideas of amplitude orderings for different components for the FLR fields no longer hold. The bottom panels (e) and (f) are taken from the 2-D FLR region closer to dusk (labeled 3 in Figure 2c at $(x, y, z) = (1.08, 8.37, 0.0)$). Here, the fast mode is much weaker (as can be seen from Figure 2b) and therefore $u_\phi \gg u_r$ based on the FLR fields dominating the signals. This is borne out by the hodograms on the right in Figure 3f), aligning with the ϕ-direction.

Overall, the key results from the simulation are:

1. A strong fast mode substantially affects the time series and hodograms (compare top and bottom panels)
2. The intermediate polarization causes significant FLR contributions to the radial velocity, which changes how we have to think about the contribution of each component to fast/Alfvén waves
3. In the 3-D FLR region, a linear velocity hodogram results

From the FAC structure and previous theory, we understand that the plasma displacement is aligned with the ridges in Figure 2c as well as the selected paths from the Resonance Map (Figure 2d). We can therefore better isolate the FLR response by rotating the perpendicular components into a local coordinate system, with one direction along the ridge and another perpendicular to it. This is discussed at length in Wright and Elsden (2016), who used coordinates $(\alpha, \beta) = (r, \phi)$ in the equatorial plane. Here, we maintain the same notation for consistency, and write the coordinate rotation as $(r, \phi) \to (\alpha', \beta')$ (with β' along the resonant ridge locally and α' across it). We investigate the angle that the hodogram makes with the ϕ direction as an indication of the FLR polarization.

Figure 4 displays each of the velocity time series from Figure 3 (with the same numbering of the locations from Figure 2c), rotated by the angle made between the major axis of the hodogram ellipse (dashed lines in hodograms of Figure 3) and the ϕ direction. This in essence is a maximization procedure, as the major axis of the hodogram ellipse gives the direction of the maximum perturbation. By default, this will generate signals with a $\sim 90°$ phase difference, since at the time when the component along the major axis (β') is maximized, the perturbation in the perpendicular direction (α') is 0.

Figure 4a shows the rotation of the velocity components in Figure 3a by the hodogram angle measured from Figure 3b of $\theta = -9.97°$ (with the convention that θ is measured positive clockwise from the ϕ direction, therefore $\theta = 0$ corresponds to a toroidal polarization). There is a clear difference in the growth of the two components, with the black curve ($u_{\beta'}$) dominated by the FLR response continuing to grow, while the red curve ($u_{\alpha'}$) saturates much earlier. Figure 4b shows the same coordinate rotation performed on the time series from Figure 3c by the hodogram angle from Figure 3d of $\theta = -30.25°$. There is a stark difference here compared to panel (a), with the velocity component along the resonance (black curve $u_{\beta'}$) dominating the one across it (red curve $u_{\alpha'}$). The polarization angle inferred from the hodogram in Figure 3d agrees well with that measured from the inclination
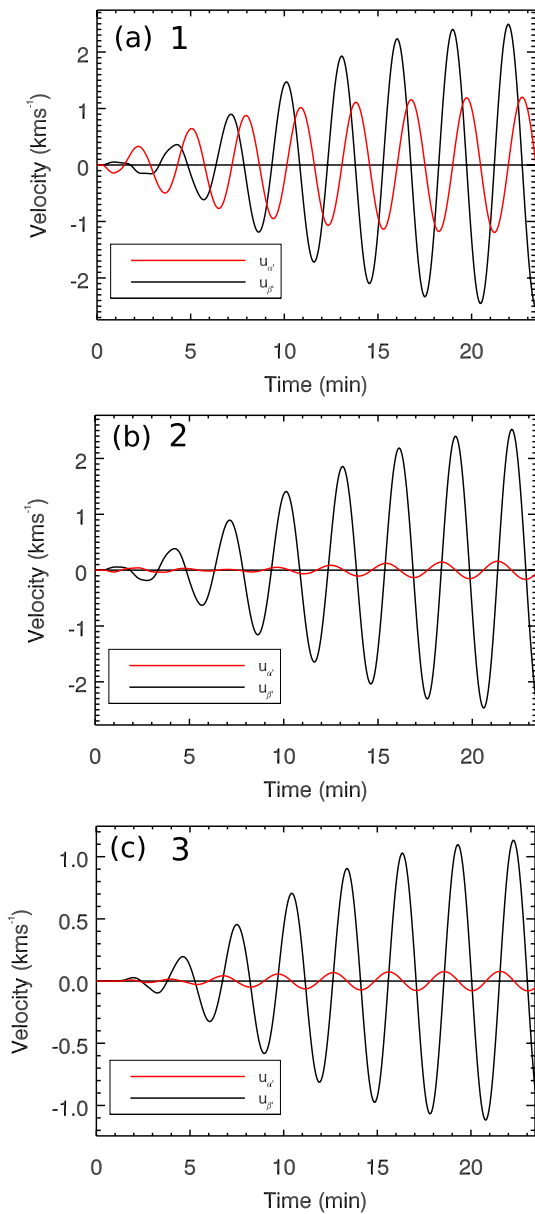
Figure 4. Time series of the velocity components from Figure 3, rotated by the hodogram angle θ. Rotated components $u_{\alpha'}$ (red) and $u_{\beta'}$ (black) are described in the main text. Locations: $(x, y, z) =$ (a) (8.20, 2.01, 0.0), (b) (6.85, 3.57, 0.0), (c) (1.08, 8.37, 0.0) (these are also marked by numbers referring to these locations in Figure) 2(c). Rotation angles: (a) $\theta = -9.97°$, (b) $\theta = -30.25°$, (c) $\theta = -2.21°$.

of the resonant contours of FAC density in Figure 2c. Furthermore, it agrees with that calculated from solutions to the Alfvén wave equation for the given location and driving frequency. Figure 4c shows the rotation of the signals of the FLR nearer dusk from Figure 3e. The hodogram angle here is essentially aligned with the ϕ direction ($\theta = -2.21°$), and hence the rotation barely alters the signal.
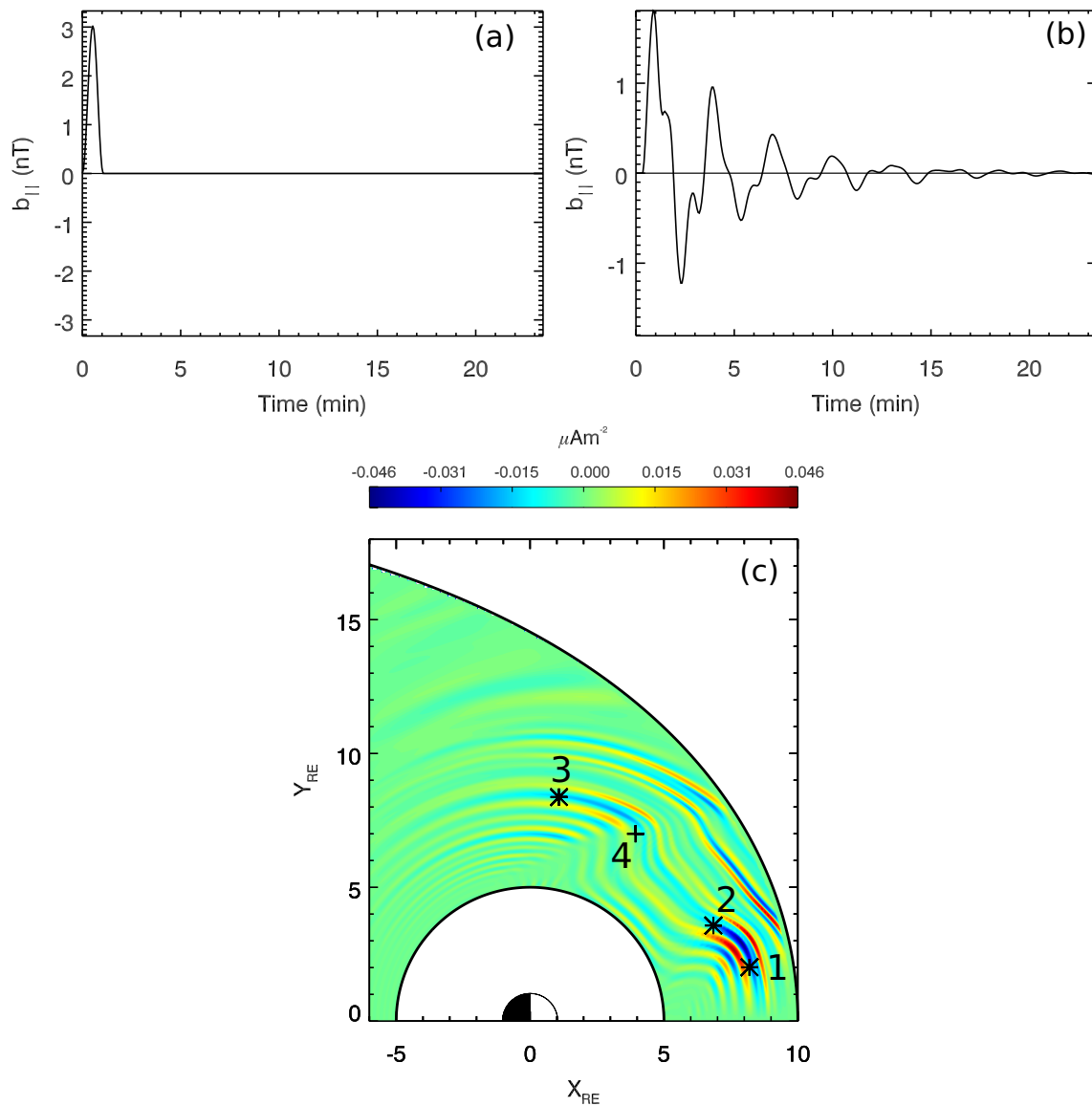
Overall these rotations provide the following information:

1. The major axis of the hodogram ellipse gives the direction of maximum wave amplitude
2. The angle created between the ϕ-direction and this major axis gives a good approximation to the FLR polarization, either at inclined 3-D FLR regions or when the FLR fields are of much larger amplitude than the fast mode fields
3. When there is a significant fast mode present, this can substantially skew the angle for example, Figures 3a and 3b, where the FLR is meant to have a toroidal polarization (angle $\theta = 0$)
4. The amount which this angle is distorted depends upon the amplitude of the fast mode (compare hodograms of Figures 3b and 3f), which also affects the width of the hodogram ellipse (length of the minor axis)

3.2. Pulse Driver

We now consider a more realistically driven case, with a pulse in the magnetic pressure at the magnetopause, modeling the magnetopause response to a solar wind dynamic pressure pulse. The time dependence of the driver ($b_{\parallel}$) at the subsolar point is shown in Figure 5a, with the response in the interior of the magnetospheric waveguide at $(x, y, z) = (7.57, 0.0, 0.0)$ shown in Figure 5b. The spatial dependence of the driver is unchanged from the monochromatic simulation. The fundamental waveguide mode clearly forms the dominant response in Figure 5b, together with higher frequency harmonics. The Alfvén wave response is displayed again through the FAC density (in a similar manner to Figure 2c) shown in Figure 5c. There is an excitation of FLRs across several L-shells, but with a dominant response corresponding to driving at the fundamental waveguide frequency, as in the previous section. The numbered asterisks again denote locations, listed in the Figure caption, from where the fields will be sampled.

In a similar fashion to Figure 3, we consider time series and hodograms at the locations shown by the black asterisks in Figure 5 (c). These are displayed in Figure 6. Figure 6a displays the perpendicular velocity and field-aligned magnetic field components near noon, at the 2-D toroidal FLR, labeled 1 in Figure 5c at $(x, y, z) = (8.20, 2.01, 0.0)$. The blue curve showing $b_{\parallel}$ decays after the initial pulse, with the red curve for the radial velocity u_r displaying a similar trend. The black curve showing the azimuthal velocity u_{ϕ} grows initially, representing the FLR being driven by the fast mode. As the fast mode

driving decays, the rate of growth in u_{ϕ} reduces and then u_{ϕ} decays due to Joule heating. The hodograms taken from three intervals in the simulation given by the vertical colored dashed lines in panel (a) are displayed in panel (b). These are more closely aligned with the ϕ direction than in the previous steadily driven monochromatic case (Figure 3b), due to the smaller amplitude fast mode here relative to the FLR amplitude, particularly in the later stages. The width of the ellipse also narrows in time, again indicative of the decay of the fast mode.

Figure 6c gives the time series from the inclined 3-D FLR (labeled 2 in Figure 5c) at $(x, y, z) = (6.85, 3.57, 0.0)$. The blue curve for $b_{\parallel}$ is similar to that in panel (a), however, the red curve for the radial velocity now bears more of a similarity to the azimuthal velocity response. This is clearly because u_r now contains a substantial

Figure 5. Pulse driven simulation: (a) $b_{\parallel}$ at the subsolar point, showing the pulse used to drive the simulation; (b) Resulting response in $b_{\parallel}$ in the waveguide interior at noon in the equatorial plane ((x, y, z) = (7.57, 0.0, 0.0)); (c) Field-aligned current $j_{\parallel}$ at the ionospheric end of the field line mapped to the equatorial plane. Black asterisks at (1): (x, y, z) = (8.20, 2.01, 0.0); (2): (6.85, 3.57, 0.0); (3): (1.08, 8.37, 0.0) and black cross (labeled 4) at (x, y, z) = (3.94, 7.0, 0.0) are locations for further analysis.

contribution from the FLR response due to the polarization of the resonance being intermediate between the radial and azimuthal directions. The hodograms in panel (d) also demonstrate this, with a more linear than elliptical shape as found in the monochromatic case also. It is further interesting how the orientation of the hodogram changes slightly over time to create a larger angle with the ϕ direction (compare purple to orange hodograms). This represents a decay of the fast mode affecting the maximum amplitude direction, which at later times is directly aligned with the large amplitude ridges in the FAC shown in Figure 5c.

The bottom panels show the response at the dusk-side FLR outside of the plume, at (x, y, z) = (1.08, 8.37, 0.0) (labeled 3 in Figure 5c). Compared to the top panels, it can be seen that there is a much smaller amplitude signal in the radial velocity at dusk, as expected by the smaller amplitude fast mode here in general. This is also aided by the fast mode at this location most likely not showing up strongly in the radial velocity due to the location sampled being on the flanks. The hodograms, therefore, are aligned dominantly with the ϕ direction. Overall, despite the
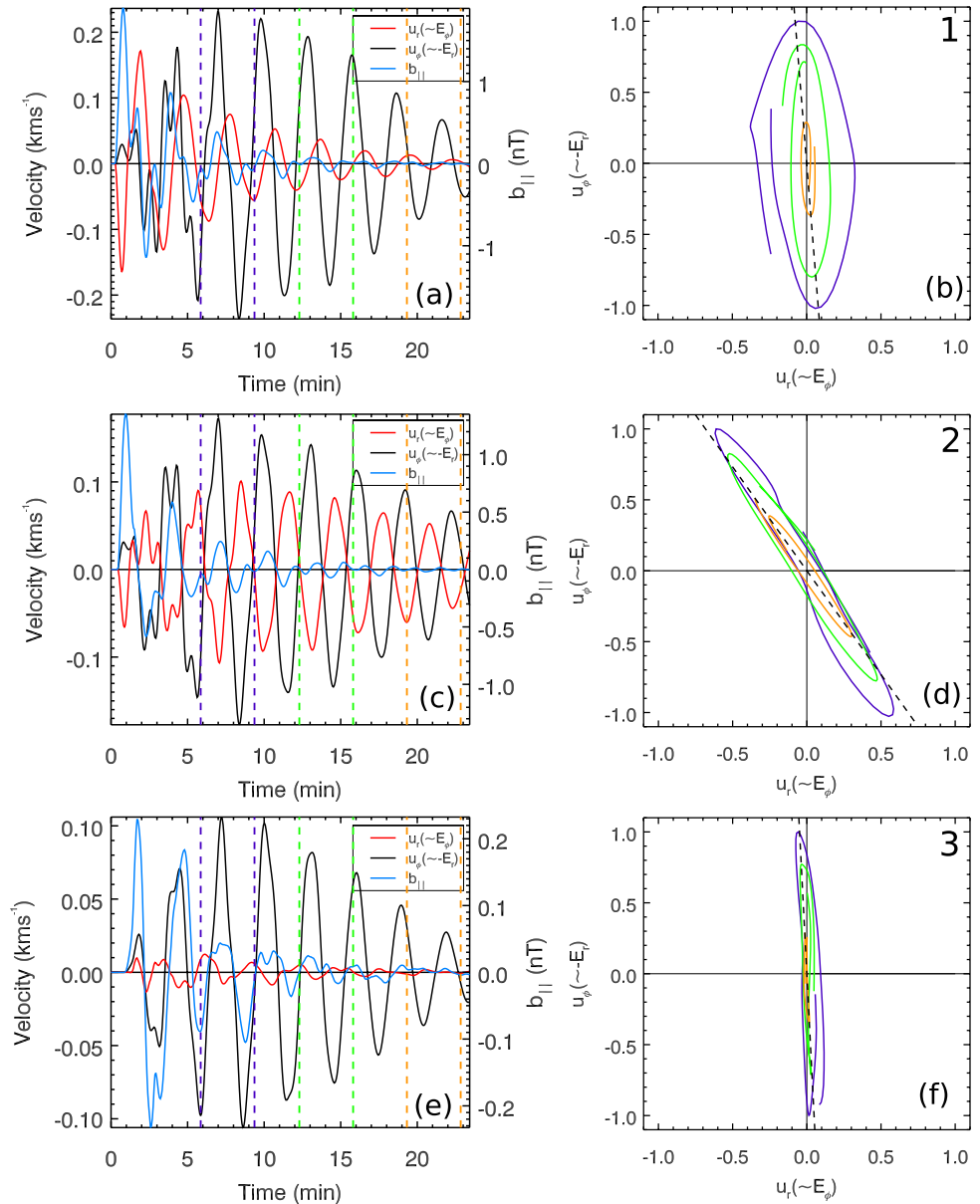
Figure 6. Time series and hodograms from the pulse driven simulation: (a) time series for u_r (red), u_ϕ (black), $b_\parallel$ (blue) at $(x, y, z) = (8.20, 2.01, 0.0)$; location nearest noon labeled 1 in Figure 5c); (b) Hodograms for perpendicular velocity components u_r and u_ϕ, with colors corresponding to the time intervals given by the dashed lines in (a); (c, d) Same as (a, b) for location $(x, y, z) = (6.85, 3.57, 0.0)$ in the inclined FLR region, labeled 2 in Figure 5c; (e, f) Same as (a, b) for location $(x, y, z) = (1.08, 8.37, 0.0)$ at the dusk side FLR, labeled 3 in Figure 5c. Dashed black lines on the hodograms give the hodogram ellipse major axis for the orange time interval.

very different driving mechanism, the hodograms bear much similarity to those of the monochromatic case. The results can be summarized by the following key points:

1. Pulse driving results in a weaker fast mode signal at later times. Therefore the signals represent the situations where the FLR responses dominate
2. At the inclined FLR region, this results in the FLR response being split between the radial and azimuthal velocity components

Figure 7 displays the perpendicular velocity components from the 3-D FLR region (from Figure 6c), rotated by the hodogram angle from Figure 6d of $\theta = -34.32°$. The rotation will give the direction of maximum amplitude,
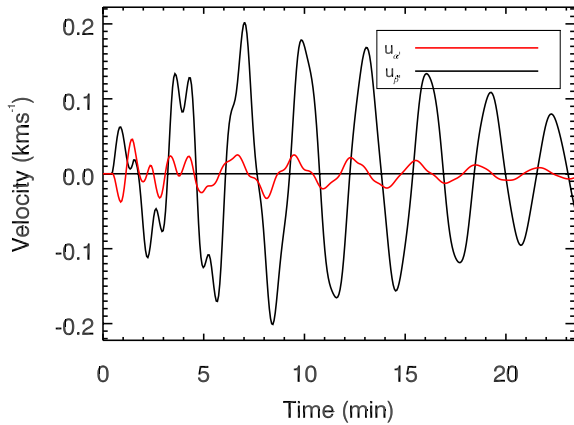
Figure 7. Rotated perpendicular velocity components at the 3-D FLR location $((x, y, z) = (6.85, 3.57, 0.0))$, indicated by the middle black asterisk labeled 2 in Figure 5(c), from the pulse driven case.

which given the decay of the fast mode by late times will highlight the direction of the FLR polarization. This can be seen by the amplitude of $u_{\beta'}$ (black) being far greater than $u_{\alpha'}$ (red).

We can also consider the satellite signatures on the duskward edge of the plume, at the location given by the black cross labeled 4 in Figure 5c $((x, y, z) = (3.94, 7.00, 0.0))$. These are shown in Figure 8a in a similar format to the previous figures. The fast mode decays (blue curve for $b_{\parallel}$) after the initial pulse. The azimuthal velocity (black) increases up to $t \sim 7$ min before decaying, while the radial velocity (red) continues to increase until $t \sim 17$ min, before decaying. By this time, the radial and azimuthal velocities are of similar amplitude. This really highlights how different the contributions to each component can be, dependent upon the location and FLR polarization.

There are a few factors at play here. At this location further round the flanks, the fast mode will have a larger contribution from u_{ϕ} than previously (where the 3-D FLR location was closer to noon). Therefore at early times $u_{\phi} \gg u_r$, since it contains both fast and FLR contributions. At this side of the plume, based on the equilibrium defined by the Alfvén speed in Figure 1b, the azimuthal Alfvén frequency gradient is slightly steeper than the noon side of the
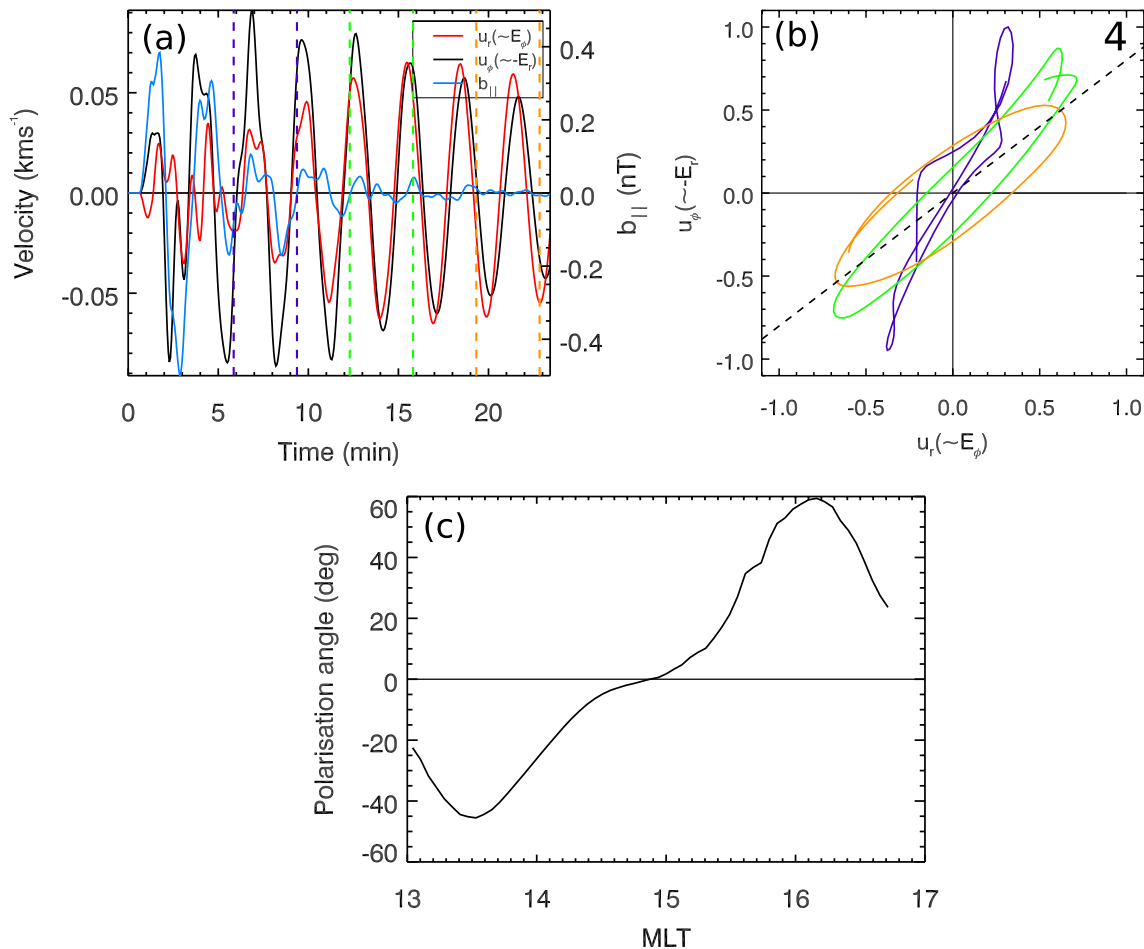
Figure 8. (a) Time series from the dusk side of the plume at $(x, y, z) = (3.94, 7.00, 0.0)$ labeled four in Figure 5c, with u_r red, u_{ϕ} black, and $b_{\parallel}$ blue. (b) Velocity hodograms from the time intervals indicated by the vertical dashed lines in (a). (c) Polarization angle (θ) variation with MLT across the plume structure measured from hodograms.

plume. This means that the FLR will be oriented at an even greater angle, and hence will give a stronger contribution to the radial velocity component.

Whereas in the 3-D FLR region on the noon side of the plume the velocity components were out of phase, here they are in phase. This can be reconciled by considering the motion of plasma back and forth along the inclined resonant contours in the FAC density from Figure 5c. On the side closer to noon, plasma will move positively azimuthally and negatively radially, and vice versa, resulting in u_r and u_ϕ being out of phase. However, on the dusk side of the plume, the radial and azimuthal motions are in phase. This is outlined by the hodograms shown in Figure 8b, which clearly have the opposite inclination to those in Figure 6d. At early times (purple), while the fast mode is still significant, the angle of the hodogram to the ϕ direction is smaller and the overall signature less clean. However by later times, a clean hodogram ellipse results with a well defined major axis (dashed line). The polarization angle here calculated from the hodogram major axis to the ϕ direction is $\theta = 51.28°$.

The predicted FLR polarization can be estimated at any MLT by considering the angle of the hodogram ellipse major axis. For a given MLT, we average the hodogram major axis angle over 1_{RE} of radial distance. This average polarization angle is plotted in the bottom panel of Figure 8 for different MLT. The hodogram polarization angle changes sign as the plume is traversed, in keeping with the previous hodograms in Figures 6d and 8b. This plot represents a key prediction to be looked for in observational data. When a plume is present, this structuring of the polarization should result and could be looked for in ground magnetometer data with the longitudinal coverage to assess structure across the plume.
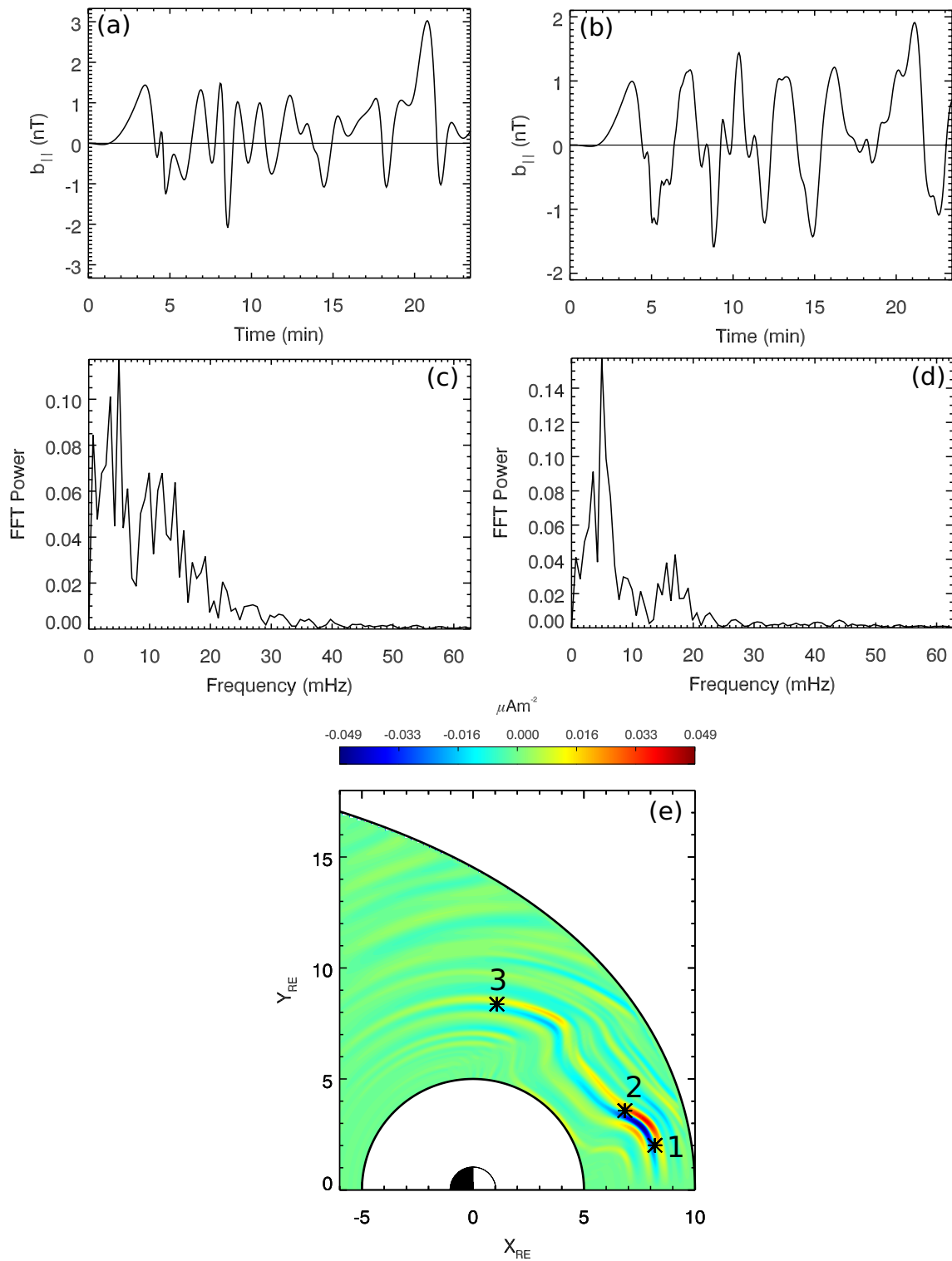
3.3. Continuous Broadband Driver

The final driver considered is that of a continuous broadband disturbance to the magnetopause boundary, indicative of random fluctuations in the solar wind dynamic pressure with a broad frequency bandwidth. The compressional magnetic field perturbation at the subsolar point used to drive the simulation is shown in Figure 9a with the corresponding fast Fourier transform (FFT) given in Figure 9c. The form of this driver was created using random discrete timesteps/amplitudes which are then connected smoothly using cubic splines. The choice of the permissible timesteps influences the resulting frequency range. In this case, there is broadband power over ~0–20 mHz. Once again, the spatial dependence of the driver is unchanged from previous cases. Figure 9b displays the compressional magnetic field response within the magnetospheric interior at $(x, y, z) = (7.57, 0, 0)$, with the FFT of this signal given in Figure 9d. The waveguide has clearly filtered the compressional disturbances (as shown by Wright & Rickard, 1995), responding most strongly with the fundamental waveguide mode (quarter radial wavelength for the given boundary conditions).

The bottom panel of Figure 9 displays the FAC density $j_\parallel$ at the ionospheric end of the field lines mapped to the equatorial plane at $t \sim 17$ min. The strongest FAC density region corresponds to the excitation of the fundamental field-aligned mode. As in previous plots, the numbered asterisks refer to locations (1: $(x, y, z) = (8.20, 2.01, 0.0)$; 2: $(6.85, 3.57, 0.0)$; 3: $(1.08, 8.37, 0.0)$) from which time series and hodograms will be plotted.
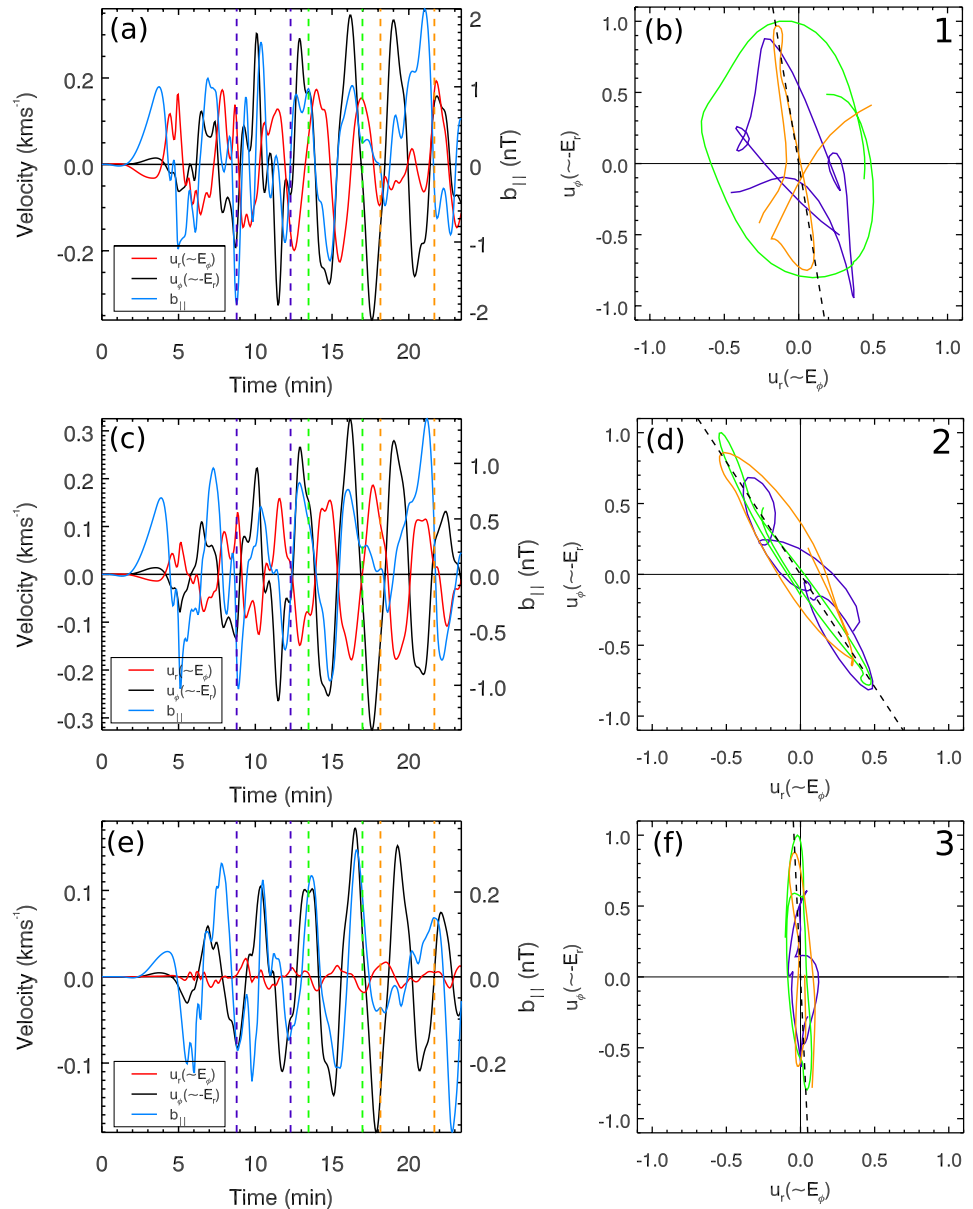
Figure 10 displays time series and hodograms for the perpendicular velocity and compressional magnetic field components from the continuously broadband driven simulation, using the same format and locations as Figures 3 and 6. The continuous broadband driving creates more noisy signals overall, however, it is remarkable how cleanly the inclined FLR polarization organizes the data. This is made clear by comparing the far more linear, inclined hodograms in panel (d) compared to those in (b). This shows that these structures are robust to more realistic forms of driving and that the predictions from the pulse driven case will carry over to this type of driving also.

There is a large positive increase in the compressional magnetic field component near the end of the simulation, clearly affecting the radial velocity also, which skews the orange hodogram in panel (b). However, the hodogram in (d) is far more resistant to this given the strength of the FLR signal in both velocity components. The data here has not been filtered, however applying a low-pass filter to isolate the fundamental waveguide mode would clean the data up substantially, as would most likely be required in observational analysis of real data. The time series and hodograms from the 2-D FLR location further round the flank shown in panels (e) and (f) again display the dominant toroidal FLR nature of the signals here, in absence of a strong fast mode.

Figure 9. Continuously broadband driven simulation: (a) driver time series for $b_{\parallel}$ at the subsolar magnetopause; (b) interior waveguide response in $b_{\parallel}$ at $(x, y, z) = (7.57, 0, 0)$; (c) FFT of the time series for the driver in (a); (d) FFT of the time series for the interior response in (b); (e) field-aligned current $j_{\parallel}$ with numbered asterisks at $(x, y, z) = $ (1): $(8.20, 2.01, 0.0)$; (2): $(6.85, 3.57, 0.0)$; (3): $(1.08, 8.37, 0.0)$ for locations used in the analysis in Figure 10.

Figure 10. Time series and hodograms from the continuously broadband driven simulation: (a) Time series for u_r (red), u_ϕ (black), $b_\parallel$ (blue) at $(x, y, z) = (8.20, 2.01, 0.0)$ (location nearest noon labeled one in Figure 9c); (b) Hodograms for perpendicular velocity components u_r and u_ϕ, with colors corresponding to the time intervals given by the dashed lines in (a); (c, d) Same as (a, b) for location $(x, y, z) = (6.85, 3.57, 0.0)$ in the inclined FLR region, labeled 2 in Figure 9c; (e, f) Same as (a, b) for location $(x, y, z) = (1.08, 8.37, 0.0)$ at the dusk side FLR, labeled 3 in Figure 9c. Dashed black lines on the hodograms give the hodogram ellipse major axis from the orange time interval.

4. Conclusions

We have performed numerical simulations of the formation of 3-D FLRs (polarization between toroidal and poloidal) in the presence of a dense plasmaspheric drainage plume on the dusk flank. Such a density structure provides significant azimuthal asymmetry, which reveals the 3-D nature of the FLR. We have investigated in detail the signatures of the magnetic and velocity fields at these 3-D FLR regions for three different forms of magnetopause driving: monochromatic, pressure pulse, and continuous broadband fluctuations. In each of the simulations, the driving excites the normal fast waveguide modes of the given equilibrium, which then drive FLRs, with a strong response occurring at the sharp azimuthal density gradients. The FLRs generate a strong FAC, showing in general

how externally imposed global compressions of the magnetopause excite local FACs through this MHD wave process. The robust nature of this response at the sharp density gradients to different forms of driving suggests that 3-D FLRs will form efficiently at steep azimuthal gradients in the Alfvén frequency. The time evolution of the fast mode is very different between each simulation, however, which results in different amplitude and phase relations between the magnetic and velocity field components.

3-D FLRs will contain a mixture of azimuthal and radial components, with the amplitude of each varying depending upon the FLR orientation. In the case where the FLR amplitude is much greater than the fast mode amplitude, the FLR polarization can be reliably estimated using the hodogram ellipse for the perpendicular field components (velocity, magnetic or electric). The major axis of the hodogram gives the direction of maximum amplitude, which in the case of the FLR fields being of larger amplitude than the fast fields, gives the FLR polarization. We have shown the effectiveness of this by rotating coordinates to this direction of maximum amplitude and showing the clear separation into FLR and fast components.

When the fast wavefield components (e.g., radial velocity near noon and field-aligned magnetic field) are of the order of the FLR fields, it is surprising how well the 3-D FLRs still order the signals. At the 2-D FLR regions (toroidal FLRs) close to noon, the presence of the fast mode broadens the hodogram ellipse and skews the major axis angle slightly. This is unsurprising, as the hodogram major axis only gives the direction of maximum amplitude. At the strongly 3-D regions however, approximately linear hodograms result for all cases of driving (Figures 3d, 6d, 10d). This leads to two key predictions to be looked for in data:

1. In 3-D FLR regions, the perpendicular field components are approximately in/out of phase which results in a linear hodogram
2. The FLR polarization should vary across the plume structure according to Figure 8c, which could be looked for in ground magnetometer data with appropriate longitudinal coverage

The 3-D FLR regime further highlights the difficulty in using a field-aligned coordinate system and ascribing meaning to each of the components in terms of individual poloidal/toroidal modes, and therefore likely generation mechanisms. 3-D FLRs provide an alternative description when there is significant amplitude in each component direction. The potential for FLRs to form efficiently at intermediate polarizations will also have implications for the acceleration of radiation belt particles. Given how different wave polarizations interact differently with drifting particles (Elkington et al., 1999; Kabin, Rankin, Mann, et al., 2007; Kabin, Rankin, Waters, et al., 2007), the 3-D nature of FLRs needs to be fully taken into account.

Data Availability Statement

Data used to produce the simulation figures can be accessed at: https://figshare.com/authors/Tom_Elsden/4743264.

References

Allan, W., Poulter, E. M., & White, S. P. (1986). Hydromagnetic wave coupling in the magnetosphere—Plasmapause effects on impulse-excited resonances. *Planetary and Space Science*, *34*, 1189–1200. https://doi.org/10.1016/0032-0633(86)90056-5

Allan, W., White, S. P., & Poulter, E. M. (1985). Magnetospheric coupling of hydromagnetic waves—Initial results. *Geophysical Research Letters*, *12*, 287–290. https://doi.org/10.1029/GL012i005p00287

Borovsky, J. E., & Denton, M. H. (2008). A statistical look at plasmaspheric drainage plumes. *Journal of Geophysical Research: Space Physics*, *113*(A9), A09221. https://doi.org/10.1029/2007JA012994

Borovsky, J. E., Welling, D. T., Thomsen, M. F., & Denton, M. H. (2014). Long-lived plasmaspheric drainage plumes: Where does the plasma come from? *Journal of Geophysical Research: Space Physics*, *119*(8), 6496–6520. https://doi.org/10.1002/2014JA020228

Chen, L., & Hasegawa, A. (1974). A theory of long-period magnetic pulsations: 1. Steady state excitation of field line resonance. *Journal of Geophysical Research*, *79*, 1024–1032. https://doi.org/10.1029/JA079i007p01024

Claudepierre, S. G., Toffoletto, F. R., & Wiltberger, M. (2016). Global MHD modeling of resonant ULF waves: Simulations with and without a plasmasphere. *Journal of Geophysical Research: Space Physics*, *121*(1), 227–244. https://doi.org/10.1002/2015JA022048

Cummings, W. D., O'Sullivan, R. J., & Coleman, P. J. Jr. (1969). Standing Alfvén waves in the magnetosphere. *Journal of Geophysical Research*, *74*(3), 778–793. https://doi.org/10.1029/JA074i003p00778

Degeling, A. W., Rae, I. J., Watt, C. E. J., Shi, Q. Q., Rankin, R., & Zong, Q. G. (2018). Control of ULF wave accessibility to the inner magnetosphere by the convection of plasma density. *Journal of Geophysical Research: Space Physics*, *123*(2), 1086–1099. https://doi.org/10.1002/2017JA024874

Degeling, A. W., Rankin, R., Kabin, K., Rae, I. J., & Fenrich, F. R. (2010). Modeling ULF waves in a compressed dipole magnetic field. *Journal of Geophysical Research: Space Physics*, *115*, A10212. https://doi.org/10.1029/2010JA015410

Dungey, J. W. (1954). *Electrodynamics of the outer atmosphere: Report to national science foundation on work carried on under grant NSF-G450*. Pennsylvania State University, Ionosphere Research Laboratory. Retrieved from https://books.google.co.uk/books?id=3NrUAAAAMAAJ

Elkington, S. R., Hudson, M. K., & Chan, A. A. (1999). Acceleration of relativistic electrons via drift-resonant interaction with toroidal-mode Pc-5 ULF oscillations. *Geophysical Research Letters*, *26*(21), 3273–3276. https://doi.org/10.1029/1999GL003659

Elkington, S. R., Hudson, M. K., & Chan, A. A. (2003). Resonant acceleration and diffusion of outer zone electrons in an asymmetric geomagnetic field. *Journal of Geophysical Research: Space Physics*, *108*(A3), 1116. https://doi.org/10.1029/2001JA009202

Ellington, S. M., Moldwin, M. B., & Liemohn, M. W. (2016). Local time asymmetries and toroidal field line resonances: Global magnetospheric modeling in SWMF. *Journal of Geophysical Research: Space Physics*, *121*(3), 2033–2045. https://doi.org/10.1002/2015JA021920

Elsden, T., & Wright, A. N. (2017). The theoretical foundation of 3-D Alfvén resonances: Time-dependent solutions. *Journal of Geophysical Research: Space Physics*, *122*, 3247–3261. https://doi.org/10.1002/2016JA023811

Goldstein, J., Sandel, B. R., Forrester, W. T., Thomsen, M. F., & Hairston, M. R. (2005). Global plasmasphere evolution 22–23 April 2001. *Journal of Geophysical Research: Space Physics*, *110*(A12), A12218. https://doi.org/10.1029/2005JA011282

Hartinger, M., Angelopoulos, V., Moldwin, M. B., Glassmeier, K.-H., & Nishimura, Y. (2011). Global energy transfer during a magnetospheric field line resonance. *Geophysical Research Letters*, *38*, L12101. https://doi.org/10.1029/2011GL047846

Jacobs, J. A., Kato, Y., Matsushita, S., & Troitskaya, V. A. (1964). Classification of geomagnetic micropulsations. *Journal of Geophysical Research*, *69*, 180–181. https://doi.org/10.1029/JZ069i001p00180

Kabin, K., Rankin, R., Mann, I. R., Degeling, A. W., & Marchand, R. (2007). Polarization properties of standing shear Alfvén waves in non-axisymmetric background magnetic fields. *Annales Geophysicae*, *25*, 815–822. https://doi.org/10.5194/angeo-25-815-2007

Kabin, K., Rankin, R., Waters, C., Marchand, R., Donovan, E., & Samson, J. (2007). Different eigenproblem models for field line resonances in cold plasma: Effect on magnetospheric density estimates. *Planetary and Space Science*, *55*(6), 820–828. https://doi.org/10.1016/j.pss.2006.03.014

Kageyama, A., Sugiyama, T., Watanabe, K., & Sato, T. (2006). A note on the dipole coordinates. *Computers & Geosciences*, *32*, 265–269. https://doi.org/10.1016/j.cageo.2005.06.006

Kivelson, M. G., & Southwood, D. J. (1985). Resonant ULF waves—A new interpretation. *Geophysical Research Letters*, *12*, 49–52. https://doi.org/10.1029/GL012i001p00049

Kivelson, M. G., & Southwood, D. J. (1986). Coupling of global magnetospheric MHD eigenmodes to field line resonances. *Journal of Geophysical Research*, *91*, 4345–4351. https://doi.org/10.1029/JA091iA04p04345

Klimushkin, D. Y., Leonovich, A. S., & Mazur, V. A. (1995). On the propagation of transversally small-scale standing Alfven waves in a three-dimensionally inhomogeneous magnetosphere. *Journal of Geophysical Research*, *100*(A6), 9527–9534. https://doi.org/10.1029/94JA03233

Lee, D.-H., & Lysak, R. L. (1989). Magnetospheric ULF wave coupling in the dipole model—The impulsive excitation. *Journal of Geophysical Research*, *94*, 17097–17103. https://doi.org/10.1029/JA094iA12p17097

Lee, D.-H., Lysak, R. L., & Song, Y. (2000). Field line resonances in a nonaxisymmetric magnetic field. *Journal of Geophysical Research*, *105*(A5), 10703–10711. https://doi.org/10.1029/1999JA000295

Leonovich, A. S., & Mazur, V. A. (1993). A theory of transverse small-scale standing Alfvén waves in an axially symmetric magnetosphere. *Planetary and Space Science*, *41*(9), 697–717. https://doi.org/10.1016/0032-0633(93)90055-7

Lu, J. Y., Wang, W., Rankin, R., Marchand, R., Lei, J., Solomon, S. C., et al. (2008). Electromagnetic waves generated by ionospheric feedback instability. *Journal of Geophysical Research: Space Physics*, *113*(A5). https://doi.org/10.1029/2007JA012659

Mathie, R. A., & Mann, I. R. (2000). Observations of Pc5 field line resonance azimuthal phase speeds: A diagnostic of their excitation mechanism. *Journal of Geophysical Research*, *105*, 10713–10728. https://doi.org/10.1029/1999JA000174

Milan, S. E., Sato, N., Ejiri, M., & Moen, J. (2001). Auroral forms and the field-aligned current structure associated with field line resonances. *Journal of Geophysical Research*, *106*(A11), 25825–25833. https://doi.org/10.1029/2001JA900077

Moldwin, M. B., Zou, S., & Heine, T. (2016). The story of plumes: The development of a new conceptual framework for understanding magnetosphere and ionosphere coupling. *Annales Geophysicae*, *34*(12), 1243–1253. https://doi.org/10.5194/angeo-34-1243-2016

Radoski, H. R. (1967). A note on oscillating field lines. *Journal of Geophysical Research*, *72*, 418–419. https://doi.org/10.1029/JZ072i001p00418

Rae, I. J., Donovan, E. F., Mann, I. R., Fenrich, F. R., Watt, C. E. J., Milling, D. K., et al. (2005). Evolution and characteristics of global Pc5 ULF waves during a high solar wind speed interval. *Journal of Geophysical Research: Space Physics*, *110*, A12211. https://doi.org/10.1029/2005JA011007

Rankin, R., Kabin, K., Lu, J. Y., Mann, I. R., Marchand, R., Rae, I. J., et al. (2005). Magnetospheric field-line resonances: Ground-based observations and modeling. *Journal of Geophysical Research: Space Physics*, *110*(A10), A10S09. https://doi.org/10.1029/2004JA010919

Russell, A. J. B., & Wright, A. N. (2010). Resonant absorption with 2-D variation of field line eigenfrequencies. *Astronomy and Astrophysics*, *511*, A17. https://doi.org/10.1051/0004-6361/200912669

Samson, J. C., Jacobs, J. A., & Rostoker, G. (1971). Latitude-dependent characteristics of long-period geomagnetic micropulsations. *Journal of Geophysical Research*, *76*, 3675–3683. https://doi.org/10.1029/JA076i016p03675

Sandel, B. R., Goldstein, J., Gallagher, D. L., & Spasojevic, M. (2003). Extreme Ultraviolet Imager Observations of the structure and dynamics of the plasmasphere. *Space Science Reviews*, *109*(1), 25–46. https://doi.org/10.1023/B:SPAC.0000007511.47727.5b

Sarris, T. E., Liu, W., Kabin, K., Li, X., Elkington, S. R., Ergun, R., et al. (2009). Characterization of ULF pulsations by THEMIS. *Geophysical Research Letters*, *36*(4), L04104. https://doi.org/10.1029/2008GL036732

Sarris, T. E., Liu, W., Li, X., Kabin, K., Talaat, E. R., Rankin, R., et al. (2010). THEMIS observations of the spatial extent and pressure-pulse excitation of field line resonances. *Geophysical Research Letters*, *37*(15), L15104. https://doi.org/10.1029/2010GL044125

Shue, J. H., Chao, J. K., Fu, H. C., Russell, C. T., Song, P., Khurana, K. K., & Singer, H. J. (1997). A new functional form to study the solar wind control of the magnetopause size and shape. *Journal of Geophysical Research*, *102*(A5), 9497–9511. https://doi.org/10.1029/97JA00196

Singer, H. J., Southwood, D. J., Walker, R. J., & Kivelson, M. G. (1981). Alfven wave resonances in a realistic magnetospheric magnetic field geometry. *Journal of Geophysical Research*, *86*, 4589–4596. https://doi.org/10.1029/JA086iA06p04589

Southwood, D. J. (1974). Some features of field line resonances in the magnetosphere. *Planetary and Space Science*, *22*, 483–491. https://doi.org/10.1016/0032-0633(74)90078-6

Southwood, D. J., Dungey, J. W., & Etherington, R. J. (1969). Bounce resonant interaction between pulsations and trapped particles. *Planetary and Space Science*, *17*(3), 349–361. https://doi.org/10.1016/0032-0633(69)90068-3

Streltsov, A. V., & Huba, J. D. (2015). Magnetospheric resonances at low and middle latitudes. *Journal of Geophysical Research: Space Physics*, *120*(9), 7718–7727. https://doi.org/10.1002/2015JA021532

Takahashi, K., & McPherron, R. L. (1984). Standing hydromagnetic oscillations in the magnetosphere. *Planetary and Space Science*, *32*, 1343–1359. https://doi.org/10.1016/0032-0633(84)90078-3

Walker, A. D. M., Greenwald, R. A., Stuart, W. F., & Green, C. A. (1979). STARE auroral radar observations of Pc5 geomagnetic pulsations. *Journal of Geophysical Research*, *84*, 3373–3388. https://doi.org/10.1029/JA084iA07p03373

Wright, A. N., & Elsden, T. (2016). The Theoretical foundation of 3-D Alfvén resonances: Normal modes. *The Astrophysical Journal*, *833*, 230. https://doi.org/10.3847/1538-4357/833/2/230

Wright, A. N., & Elsden, T. (2020). Simulations of MHD wave propagation and coupling in a 3-D magnetosphere. *Journal of Geophysical Research: Space Physics*, *125*(2), e27589. https://doi.org/10.1029/2019JA027589

Wright, A. N., & Rickard, G. J. (1995). A numerical study of resonant absorption in a magnetohydrodynamic cavity driven by a broadband spectrum. *Astrophysical Journal*, *444*, 458–470. https://doi.org/10.1086/175620

Wright, A. N., & Thompson, M. J. (1994). Analytical treatment of Alfvén resonances and singularities in nonuniform magnetoplasmas. *Physics of Plasmas*, *1*, 691–705. https://doi.org/10.1063/1.870815

Zalesak, S. T. (1979). Fully multidimensional flux-corrected transport algorithms for fluids. *Journal of Computational Physics*, *31*, 335–362. https://doi.org/10.1016/0021-9991(79)90051-2